Energy & Environmental Science

Stable and Selective Electrosynthesis of Hydrogen Peroxide and the Electro-Fenton Process on $CoSe_2$ Polymorph Catalysts

Journal:	*Energy & Environmental Science*
Manuscript ID	EE-ART-06-2020-001925.R1
Article Type:	Paper
Date Submitted by the Author:	03-Aug-2020
Complete List of Authors:	Sheng, Hongyuan; University of Wisconsin-Madison, Department of Chemistry Janes, Aurora; University of Wisconsin-Madison, Department of Chemistry Ross, R.; University of Wisconsin-Madison, Department of Chemistry Kaiman, Dave; University of Wisconsin-Madison, Department of Chemistry Huang, Jinzhen; University of Wisconsin-Madison, Department of Chemistry; Harbin Institute of Technology, Center for Composite Materials and Structures Song, Bo; University of Wisconsin-Madison, Department of Chemistry; Harbin Institute of Technology, Center for Composite Materials and Structures Schmidt, J.; University of Wisconsin-Madison, Department of Chemistry Jin, Song; University of Wisconsin-Madison, Department of Chemistry

ARTICLE

Stable and Selective Electrosynthesis of Hydrogen Peroxide and the Electro-Fenton Process on $CoSe_2$ Polymorph Catalysts†

Received 00th January 20xx,
Accepted 00th January 20xx

DOI: 10.1039/x0xx00000x

Hongyuan Sheng,‡[a] Aurora N. Janes,‡[a] R. Dominic Ross,[a] Dave Kaiman,[a] Jinzhen Huang,[a,b] Bo Song,[a,b] J. R. Schmidt,*[a] and Song Jin*[a]

Electrochemical synthesis of hydrogen peroxide (H_2O_2) in acidic solution can enable the electro-Fenton process for decentralized environmental remediation, but robust and inexpensive electrocatalysts for the selective two-electron oxygen reduction reaction ($2e^-$ ORR) are lacking. Here, we present a joint computational/experimental study that shows both structural polymorphs of earth-abundant cobalt diselenide (orthorhombic *o*-$CoSe_2$ and cubic *c*-$CoSe_2$) are stable against surface oxidation and catalyst leaching due to the weak O* binding to Se sites, highly active and selective for $2e^-$ ORR, and deliver higher kinetic current densities for H_2O_2 production than the state-of-the-art noble metal or single-atom catalysts in acidic solution. *o*-$CoSe_2$ nanowires directly grown on carbon paper electrodes allow for the steady bulk electrosynthesis of H_2O_2 in 0.05 M H_2SO_4 with a practically useful accumulated concentration of 547 ppm, the highest among the reported $2e^-$ ORR catalysts in acidic solution. Such efficient and stable H_2O_2 electrogeneration further enables the effective electro-Fenton process for model organic pollutant degradation.

Broader context

Hydrogen peroxide (H_2O_2) is an eco-friendly oxidant, but its centralized chemical production method poses significant cost, energy consumption, and safety concerns. Decentralized electrosynthesis using renewable electricity to selectively reduce O_2 to H_2O_2 could better satisfy end-user demands without hazardous transportation, yet robust, earth-abundant catalysts that are active in acidic solution and readily couple with the electro-Fenton process for on-site environmental remediation are lacking. Here, we combine computations and experiments to establish cobalt diselenide polymorphs as stable and selective electrocatalysts for H_2O_2 synthesis in acidic solution, enabling the steady accumulation of a practically useful H_2O_2 concentration and the effective electro-Fenton degradation of a model organic pollutant. This joint study establishes new benchmark catalysts and reveals new mechanistic insights and design rules for stable metal compound catalysts for on-site H_2O_2 production.

Introduction

Hydrogen peroxide (H_2O_2) is a versatile and green oxidant with a myriad of applications in industrial, environmental, healthcare, and household settings. It is among the list of disinfectants for use against SARS-CoV-2, a novel coronavirus that causes the COVID-19 pandemic.[1] The annual global production of H_2O_2 reached over 5 million tons in 2015 and has been steadily growing,[2] the majority of which is produced via the indirect anthraquinone process.[3] This energy- and waste-intensive multistep process relies on centralized chemical plants and produces up to 70 wt% concentrated solutions of H_2O_2 that are both hazardous and expensive to store and transport to end-users.[3] Although such centralized H_2O_2 production may benefit large-scale industrial applications,[2] many distributed applications including water treatment, medical disinfection, and household sanitation require only very low concentrations of H_2O_2. For example, a concentration less than 1000 ppm (29 mM) is sufficient for water treatment.[4] This motivates alternative approaches to the direct and decentralized production of dilute H_2O_2 at the point of use.[4-7] While direct chemical synthesis of H_2O_2 from H_2 and O_2 gases could be a potential alternative production method, it still needs H_2 gas and must operate under large quantities of inert carrier gas and solvent due to flammability concerns, and very few noble metal alloy catalysts show satisfactory selectivity toward H_2O_2 production as opposed to decomposition and/or further reduction to H_2O.[8, 9]

Direct electrochemical synthesis of H_2O_2 from the two-electron oxygen reduction reaction ($2e^-$ ORR) offers a more sustainable solution to decentralized manufacturing.[4-7] It can be driven by the increasingly affordable renewable electricity[10, 11] and eliminates the need for H_2 gas (which requires significant energy to produce from steam methane reforming and has a large carbon footprint[12]). The key challenge here is to develop robust electrocatalysts featuring high activity and selectivity toward the $2e^-$ (vs. the competing $4e^-$) ORR pathway. Defective[13-15] and heteroatom-doped[16-18] carbon materials

[a] Department of Chemistry, University of Wisconsin–Madison, 1101 University Avenue, Madison, Wisconsin 53706, United States
[b] Center for Composite Materials and Structures, Harbin Institute of Technology, Harbin 150001, China
† Electronic Supplementary Information (ESI) available. See DOI: 10.1039/x0xx00000x
‡ These authors contributed equally.
* Corresponding author: schmidt@chem.wisc.edu (J.R.S.); jin@chem.wisc.edu (S.J.)

have shown promise for the selective 2e$^-$ ORR in *alkaline* solution ($O_2 + H_2O + 2\ e^- \rightarrow HO_2^- + OH^-$, E^o = 0.76 V vs. RHE); however, H_2O_2 is unstable in base especially at pH >9,[7] and the 2e$^-$ ORR *activities* of carbon materials under acidic and neutral conditions are inferior to those under alkaline conditions, which is still the case after introducing transition metal single-atom coordination motifs into the carbon matrices.[19-23]

The electrosynthesis of H_2O_2 in *acidic* solution ($O_2 + 2\ H^+ + 2\ e^- \rightarrow H_2O_2$, E^o = 0.69 V vs. RHE) would also be advantageous for on-site water disinfection and environmental treatment applications.[7] For example, the electro-Fenton process operates at an optimal pH of ~3, where the electrogenerated H_2O_2 at the cathode reacts with Fe^{2+} and produces hydroxyl radical (·OH) as an even more potent oxidant for the removal of a wide variety of persistent organic pollutants from wastewater streams. Compared to the conventional *chemical* Fenton process, the *electro*-Fenton process not only avoids the transportation and storage of hazardous H_2O_2 but also features significantly enhanced ·OH production rates and organics mineralization capabilities because of the rapid regeneration of Fe^{2+} at the cathode.[24] However, the cathode used for the electro-Fenton process has been almost exclusively carbon materials to date,[25] which suffer from insufficient catalytic activity for H_2O_2 production in acidic solution. The state-of-the-art 2e$^-$ ORR electrocatalysts under acidic conditions are based on noble metal alloys,[26, 27] which are not commercially viable as they involve expensive and/or toxic metals (such as Hg). Therefore, developing efficient and cost-effective 2e$^-$ ORR catalysts for the electrosynthesis of H_2O_2 in acidic solution remains an important but relatively underexplored target.

Our recent work has demonstrated the promise of earth-abundant transition metal compound electrocatalysts for the selective 2e$^-$ ORR in acidic solution.[28] The unique structural motifs of metal compounds, such as cobalt disulfide (CoS_2), enable the intrinsic separation of active metal sites by the lattice anions, which could potentially suppress O-O bond scission by adjacent active sites and resist the undesired 4e$^-$ ORR that yields the H_2O byproduct. This motivates us to look into cobalt diselenide ($CoSe_2$), which has larger anions increasing the separation between the neighboring Co active sites, in order to achieve enhanced 2e$^-$ ORR selectivity. Selenium is also less electronegative than sulfur, which can impact the electronic structures and therefore the adsorbate binding energies and activation barriers. However, $CoSe_2$ can exist in two structural polymorphs with different crystal structures, the *cubic* pyrite-type (*c*-$CoSe_2$) and the *orthorhombic* marcasite-type (*o*-$CoSe_2$), whereas CoS_2 always exists as the *cubic* pyrite-type (*c*-CoS_2). These distinct structures of $CoSe_2$ polymorphs vs. CoS_2 can influence not only the catalyst activity and selectivity but also the catalyst stability under acidic electrochemical operations, which is critical from a practical perspective. For example, $CoSe_2$[29, 30] appears to be more electrochemically stable than CoS_2[31-33] for hydrogen evolution reaction (HER) in acidic solution.

Here, we report the stable and selective electrosynthesis of H_2O_2 and the effective electro-Fenton process on $CoSe_2$ polymorph catalysts in the more practically relevant acidic solution, due to the new understandings from both theory and experiment that lead to significantly improved catalyst stability. Theoretical calculations of bulk and surface Pourbaix diagrams reveal general mechanistic insights into the enhanced electrochemical stability of $CoSe_2$ polymorphs against surface oxidation. Computational modelling of 2e$^-$ ORR energetics also predicts them to be active and selective electrocatalysts for H_2O_2 production. Electrochemical measurements and rigorous monitoring of catalyst dissolution show that $CoSe_2$ polymorphs are the best-performing 2e$^-$ ORR catalysts reported so far in *acidic* solution and are more resistant to catalyst leaching. Remarkably, bulk electrosynthesis of H_2O_2 using *o*-$CoSe_2$ nanostructures grown on carbon paper electrode successfully accumulates a practically useful H_2O_2 concentration of 547 ppm (16 mM) in *acidic* solution, significantly higher than those achieved by previously reported catalysts in similar H-cells. The *o*-$CoSe_2$ electrode further enables the effective electro-Fenton process and the efficient degradation of recalcitrant organic pollutant, showing great promise for on-site water treatment applications.

Results and discussion

Bulk Pourbaix diagrams and Electrochemical Stability of $CoSe_2$ Polymorphs

Practical electrochemical H_2O_2 production necessitates stable electrocatalysts for the selective 2e$^-$ ORR. The crystal structures of both $CoSe_2$ polymorphs in comparison with *c*-CoS_2 are shown in Fig. 1a–c. According to the calculated bulk Pourbaix diagrams available from the Materials Project,[34, 35] the electrochemical stability window of *c*-CoS_2 is limited (Fig. S1a, ESI†), in agreement with a recent report.[36] In contrast, both $CoSe_2$ polymorphs exhibit much wider electrochemical stability windows that cover the entire potential range of interest for *acidic* 2e$^-$ ORR (Fig. S1b,c, ESI†). As such, $CoSe_2$ polymorphs are anticipated to better retain their structural integrity under acidic electrochemical operations, whereas *c*-CoS_2 is more prone to catalyst degradation due to surface oxidation and Co^{2+} dissolution. Therefore, the enhanced electrochemical stability of $CoSe_2$ polymorphs could make them more practical 2e$^-$ ORR catalysts in acidic solution for on-site water treatment applications.

Mechanistic Insights from Surface Pourbaix Diagrams of $CoSe_2$ Polymorphs

To understand these differences in the electrochemical stability of $CoSe_2$ polymorphs vs. *c*-CoS_2 and to gain general mechanistic insights, we constructed calculated surface Pourbaix diagrams to predict the most thermodynamically stable surface termination of each catalyst for a given set of potential and pH conditions under the assumption that the surfaces can be approximated in equilibrium with $H_2O_{(l)}$.[37, 38] The equilibrated proton-coupled electron transfer (PCET) reaction for a general surface intermediate can then be written as:

$$X\text{-}O_mH_n^* + (2m - n)\ (H^+ + e^-) \rightleftharpoons X^* + mH_2O \quad (1)$$

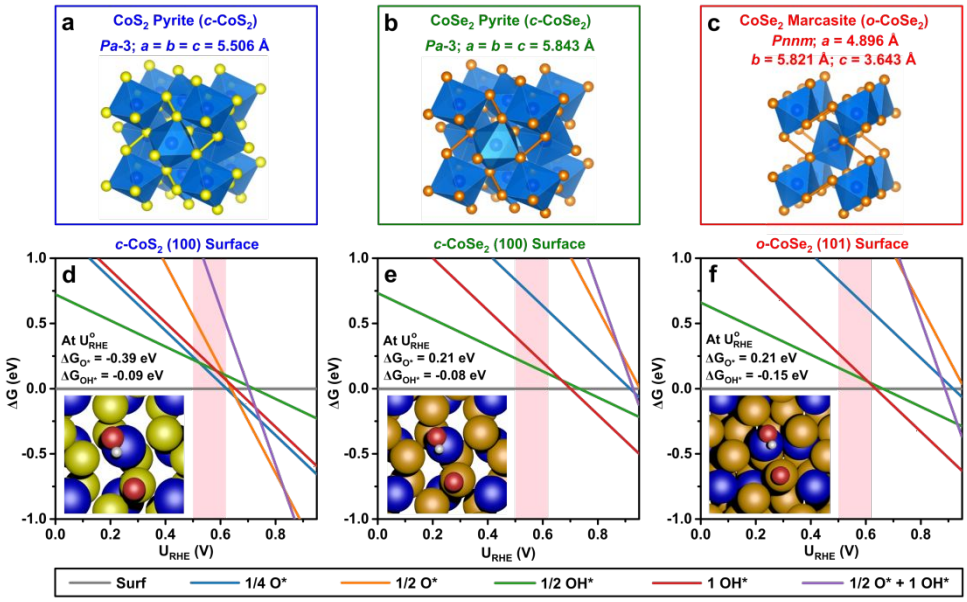

Fig. 1 Crystal structures and surface Pourbaix diagrams. (a–c) Crystal structures, space groups, and lattice constants of (a) *c*-CoS_2, (b) *c*-$CoSe_2$, and (c) *o*-$CoSe_2$. The Co, S, and Se atoms are displayed in blue, yellow, and orange, respectively. (d–f) Calculated surface Pourbaix diagrams (ΔG vs. U_{RHE}) of (d) *c*-CoS_2 (100), (e) *c*-$CoSe_2$ (100), and (f) *o*-$CoSe_2$ (101) surfaces. Co and S/Se sites are the preferential binding sites for OH* and O*, respectively. A wide variety of surface coverages (from clean surface to ¾ ML O* + 1 ML OH*) are examined. For the sake of clarity, only the most stable surface coverages in the potential range of 0 to 1 V are shown here, and all the modelled surface coverages are shown in Fig. S3 (ESI†). Surface free energies are assumed to be in equilibrium with $H_2O_{(l)}$. The unit cell has two Co binding sites and four S/Se binding sites. Binding energies of O* and OH* (ΔG_{O*} and ΔG_{OH*}) at the calculated standard equilibrium potential of 2e⁻ ORR (U^{o}_{RHE}) and top views of the catalyst surfaces with O* and OH* bound to their preferential binding sites are shown as insets. The Co, S, Se, O, and H atoms are displayed in blue, yellow, orange, red, and white, respectively. The highlighted regions in light red represent the experimentally relevant potential range where the optimal H_2O_2 production performances are achieved.

where X is the surface binding site, *m* is the number of oxygen atoms, and *n* is the number of hydrogen atoms. The free energy of this reaction can be written as:

$$\Delta G(U,pH) = G_{S*} + mG_{H_2O} - G_{X-O_mH_n*} - (2m-n)(G_{e^-} + G_{H^+}) \quad (2)$$

Using the computational hydrogen electrode (CHE) method[39-42] ($G_{e^-} + G_{H^+} = \frac{1}{2}G_{H_2} - U_{SHE} - 2.303k_BT\,pH$) and converting standard hydrogen electrode to reversible hydrogen electrode ($U_{RHE} = U_{SHE} + 2.303k_B\,T\,pH$), the free energy can be rewritten as a function of U_{RHE}:

$$\Delta G(U_{RHE}) = G_{S*} + mG_{H_2O} - G_{X-O_mH_n*} - (2m-n)(\tfrac{1}{2}G_{H_2} - U_{RHE}) \quad (3)$$

We used density functional theory (DFT) and the CHE method[39-42] to construct calculated surface Pourbaix diagrams of all three catalysts on their most thermodynamically stable facets. We found that the (100) facet of cubic *c*-$CoSe_2$ has the lowest surface energy (Table S1a, ESI†), in agreement with cubic *c*-CoS_2.[28] For orthorhombic *o*-$CoSe_2$, we investigate the (101) facet because it is not only the facet with the lowest surface energy (Table S1b, ESI†) but also keeps the Se_2^{2-} dumbbells intact and is structurally similar to the (100) facets of cubic *c*-CoS_2 and *c*-$CoSe_2$ (see Fig. S2, ESI†). We utilized a 1×1 unit cell slab of the catalyst surface that has 2 Co binding sites and 4 S/Se binding sites to model surface intermediate coverages as a function of potential (Fig. 1d–f). The preferential binding sites for O* and OH* are Co and S/Se sites, respectively (see insets of Fig. 1d–f). Therefore, we investigated ¼, ½, ¾, and 1 monolayer (ML) O* coverages, ½ and 1 ML OH* coverages, and any combinations thereof. For example, the co-adsorption of ¼ ML O* and ½ ML OH* on $CoSe_2$ polymorphs and *c*-CoS_2 in equilibrium with their clean surfaces can be written respectively as:

$$\text{Co-OH*} + \text{Se-O*} + 3(H^+ + e^-) \rightleftharpoons \text{Co*} + \text{Se*} + H_2O \quad (4)$$

$$\text{Co-OH*} + \text{S-O*} + 3(H^+ + e^-) \rightleftharpoons \text{Co*} + \text{S*} + H_2O \quad (5)$$

where OH* and O* are bound to their preferential binding site of Co and S/Se, respectively (see Equation 1 for the general form of these equations). For the sake of clarity, Fig. 1d–f only show the most thermodynamically stable surface coverages in the potential (U_{RHE}) range of 0 to 1 V, while all the modelled surface coverages are shown in Fig. S3 (ESI†). We note that the calculated standard equilibrium potential of 2e⁻ ORR (U^{o}_{RHE}) is 0.81 V, slightly higher than the experimental value (E^o) of 0.69 V. Since our experimental results show that the optimal H_2O_2 production performances are achieved at 0.5 V vs. RHE (vide infra), the experimentally relevant potential range between 0.5 and 0.62 V is highlighted in Fig. 1d–f. At 0.5 V, all surfaces are predicted to be mostly free of adsorbates. However, at the most important 0.62 V, we predict ¼ ML O* coverage on *c*-CoS_2 (Fig. 1d), a clean *c*-$CoSe_2$ surface (Fig. 1e), and 1 ML OH* coverage on *o*-$CoSe_2$ (Fig. 1f).

The differences in the surface terminations of all three catalysts under equilibrium conditions with $H_2O_{(l)}$ can be explained by the relative differences in the O* and OH* binding strengths. O* binds 0.59 eV more strongly to S sites of *c*-CoS_2

than to Se sites of $CoSe_2$ polymorphs (see ΔG_{O*} values in Fig. 1d–f). Therefore, we predict a moderate O* coverage on *c*-CoS_2 at low overpotentials (Fig. 1d), which will likely lead to surface oxidation, the formation of SO_4^{2-}, and the subsequent leaching of Co^{2+}. In contrast, O* coverage is not the most stable surface termination on $CoSe_2$ polymorphs at low overpotentials (Fig. 1e,f) because of the weak O* binding to Se sites, suggesting that $CoSe_2$ polymorphs should be more resistant to surface oxidation and catalyst degradation, consistent with their wide electrochemical stability windows in the bulk Pourbaix diagrams (Fig. S1b,c, ESI†).

While changing the nature of the anion in the catalyst modifies the binding strength of O* and leads to increased stability of $CoSe_2$ polymorphs, switching from the *cubic* to *orthorhombic* crystal structure affects the binding strength of OH* to the preferential Co binding sites. The (101) surface of orthorhombic *o*-$CoSe_2$, which has a longer Co-Co interatomic distance than the (100) surfaces of both cubic structures (Fig. S2d–f, ESI†), exhibits a slight increase in the OH* binding strength by 0.06 and 0.07 eV compared to the (100) surface of cubic *c*-CoS_2 and *c*-$CoSe_2$, respectively (see ΔG_{OH*} values in Fig. 1d–f). At low overpotentials, we predict a moderate to high OH* coverage on both $CoSe_2$ polymorphs, which will slowly decrease as the overpotential increases. As OH* binds to Co sites, a higher OH* coverage decreases the number of Co site ensembles available to break the O-O bond in OOH*. Thus, OH* coverage on Co sites may increase the $2e^-$ ORR selectivity, suggesting orthorhombic *o*-$CoSe_2$ could be more selective than cubic *c*-$CoSe_2$ and *c*-CoS_2. Overall, the surface and bulk Pourbaix diagrams predict that both $CoSe_2$ polymorphs are more electrochemically stable than *c*-CoS_2, while *o*-$CoSe_2$ could be the most intrinsically selective toward $2e^-$ ORR among all three catalysts.

Computational Prediction of Selective $2e^-$ ORR Energetics on $CoSe_2$ Polymorphs

We further calculated free energy diagrams of $2e^-$ ORR vs. the competing $4e^-$ ORR pathway to elucidate the catalytic activity and selectivity of $CoSe_2$ polymorphs. The catalytic activity toward $2e^-$ ORR is governed by the following PCET reactions:

$$O_{2(g)} + * + (H^+ + e^-) \rightarrow OOH* \quad (6)$$

$$OOH* + (H^+ + e^-) \rightarrow H_2O_{2(aq)} \quad (7)$$

where the preferential binding sites for OOH* are Co sites on all three catalysts. At the calculated standard equilibrium potential of $2e^-$ ORR (U^o_{RHE}), the first PCET step (Equation 6) is moderately downhill by 0.27, 0.24, and 0.35 eV on *c*-CoS_2 (100), *c*-$CoSe_2$ (100), and *o*-$CoSe_2$ (101) surfaces, respectively (Fig. 2), indicating that all three catalysts should be active toward $2e^-$ ORR, and *c*-$CoSe_2$ could be the most intrinsically active among all three catalysts.

While the catalytic activity of $2e^-$ ORR is determined by Equations 6 and 7, the catalytic selectivity of $2e^-$ vs. $4e^-$ ORR is set by the resistance to O-O bond scission in OOH* adsorbate:

$$OOH* \rightarrow O* + OH* \quad (8)$$

$$OOH* + * + (H^+ + e^-) \rightarrow O* + H_2O_{(l)} \quad (9)$$

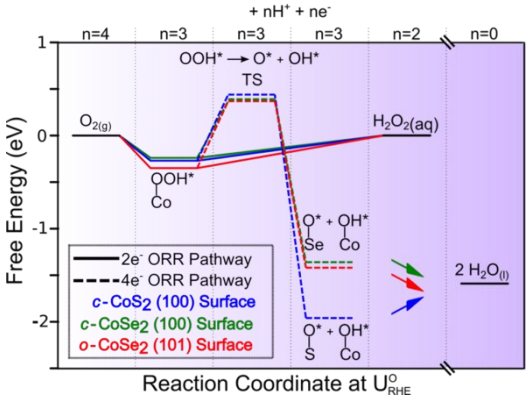

Fig. 2 Calculate free energy diagrams of $2e^-$ and $4e^-$ ORR pathways. Calculated free energy diagrams were performed on *c*-CoS_2 (100), *c*-$CoSe_2$ (100), and *o*-$CoSe_2$ (101) surfaces at the calculated standard equilibrium potential of $2e^-$ ORR (U^o_{RHE}). Possible $2e^-$ and $4e^-$ ORR pathways are depicted in solid and dashed lines, respectively. The traces for *c*-CoS_2 (100), *c*-$CoSe_2$ (100), and *o*-$CoSe_2$ (101) surfaces are displayed in blue, green, and red, respectively. These calculations are performed on clean surfaces as the binding energies of OOH* are insensitive to other surface adsorbates present on *c*-CoS_2[28] and both $CoSe_2$ polymorphs at low overpotentials (see surface Pourbaix diagrams in Fig. 1).

The cleavage of the O-O bond in OOH* will result in a buildup of O* and OH* on the catalyst surface (Equation 8). These species can either lead to oxidation/dissolution of the catalyst or be further reduced to $H_2O_{(l)}$. Breaking the O-O bond in OOH* requires an ensemble of neighboring Co sites to move toward each other, after which OOH* will dissociate into O* and OH* that are initially bound to Co sites.[28] O* can then easily migrate to S/Se sites, which are the preferential binding sites for O* on all three catalysts. Alternatively, the O-O bond in OOH* could be cleaved through reductive elimination (Equation 9) to form O* and $H_2O_{(l)}$. However, this is unlikely as only the proximal oxygen in OOH* interacts strongly with the catalyst surface. Therefore, PCET to the surface-bound oxygen to form H_2O_2 (Equation 7) will likely dominate over PCET to the distant oxygen to form $H_2O_{(l)}$ and O* (Equation 9).[28] The OOH* dissociation barriers on all three catalysts are fairly similar (Fig. 2), in agreement with the similarity of their OOH* binding energies and surface structures. The (101) surface of *o*-$CoSe_2$ exhibits a slightly higher OOH* dissociation barrier of 0.72 eV than the (100) surface of *c*-CoS_2 and *c*-$CoSe_2$ where the barrier is 0.71 and 0.63 eV, respectively (Fig. 2). These barriers to O-O bond scission on $CoSe_2$ polymorphs and CoS_2 are significantly higher than those on close-packed metals such as Pd (0.06 eV), Pt (0.16 eV), and Cu (0.06 eV),[42] indicating that spatial separation of neighboring Co sites by S/Se anions (Fig. S2, ESI†) is critical to the selective $2e^-$ ORR pathway. Overall, the calculated free energy diagrams suggest that both $CoSe_2$ polymorphs are active and selective $2e^-$ ORR catalysts and that *c*-$CoSe_2$ could be more intrinsically active while *o*-$CoSe_2$ could be more intrinsically selective.

Synthesis and Characterization of Nanostructured $CoSe_2$ Polymorph Catalysts

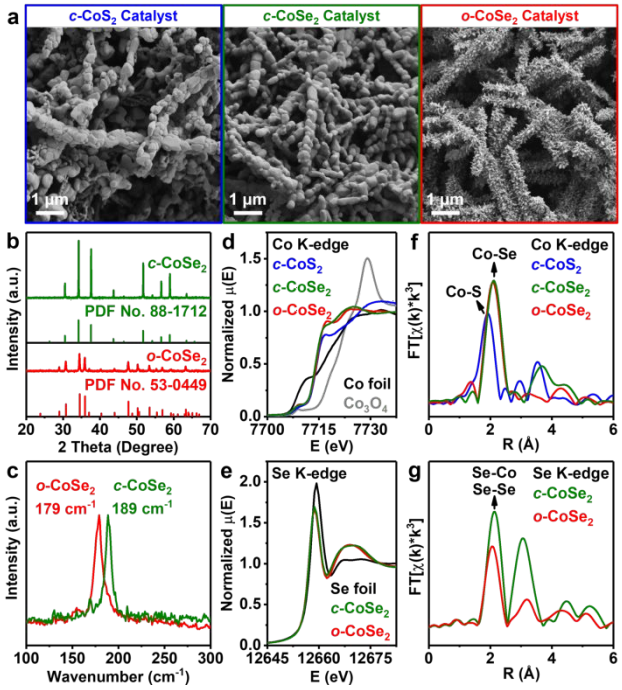

Fig. 3 Structural characterization of nanostructured *c*-$CoSe_2$ and *o*-$CoSe_2$ catalysts in comparison with *c*-CoS_2 catalyst. (a) SEM images, (b) PXRD patterns, (c) Raman spectra, (d) Co K-edge and (e) Se K-edge XANES spectra, Fourier transforms of (f) Co K-edge and (g) Se K-edge EXAFS spectra of as-synthesized *c*-$CoSe_2$, *o*-$CoSe_2$, and *c*-CoS_2 catalysts. Standard PXRD patterns of *c*-$CoSe_2$ (PDF No. 88-1712) and o-CoSe2 (PDF No. 53-0449) are from the International Centre for Diffraction Data (ICDD) database. The Co K-edge XANES spectra of Co foil and Co_3O_4 are shown in (d) and the Se K-edge XANES spectra of Se foil are shown in (e) for comparison.

We synthesized nanostructured $CoSe_2$ polymorph catalysts via hydrothermal selenization of cobalt hydroxide carbonate hydrate (CHCH) precursor at 220 °C,[43] followed by thermal annealing at higher temperatures to remove excess elemental Se impurity and to control the polymorphism of *o*-$CoSe_2$ and *c*-$CoSe_2$ at 300 and 500 °C, respectively (Fig. 3a). We also synthesized *c*-CoS_2 catalyst via vapor-phase sulfidation of CHCH precursor at 500 °C as a comparison sample.[31] The low-temperature hydrothermal selenization at 220 °C enables access to the metastable marcasite-type $CoSe_2$ that undergoes structural transformation into the pyrite-type polymorph at temperatures higher than 300 °C. Powder X-ray diffraction (PXRD) pattern confirmed the marcasite structure of as-converted $CoSe_2$ sample; however, there was *crystalline* elemental Se impurity (Fig. S4a, ESI†). After thermal annealing in Ar atmosphere (790 torr) at 300 °C, the crystalline Se impurity was eliminated while the marcasite structure was retained (Fig. 3b). The complete polymorphic transformation of marcasite- to pyrite-type $CoSe_2$ took place at a higher annealing temperature of 500 °C (Fig. 3b and S4b, ESI†). Raman spectra further confirmed the polymorphic purity of the $CoSe_2$ samples annealed at 300 and 500 °C, respectively, given their distinct Se-Se stretching mode signals at 179 vs. 189 cm^{-1} (Fig. 3c and S5a, ESI†). Additional Raman (Fig. S5b, ESI†) and X-ray photoelectron spectroscopy (XPS) characterization (Fig. S6, ESI†) also showed that, for the *o*-$CoSe_2$ sample annealed at 300 °C, an extended annealing time was necessary to completely remove residual *amorphous* elemental Se impurity without affecting the marcasite structure. Scanning electron microscopy (SEM) images showed that the 300 °C annealing retained the nanoscale morphology and surface roughness of the *o*-$CoSe_2$ sample, whereas the 500 °C annealing enlarged the grain sizes of the *c*-$CoSe_2$ sample (Fig. 3a and S7, ESI†). These structural characterization results confirmed that both $CoSe_2$ polymorph catalysts studied in this work, the *c*-$CoSe_2$ sample annealed at 500 °C for 1 h and the *o*-$CoSe_2$ sample annealed at 300 °C for 3 h, are polymorphic pure and free of elemental Se impurity (Fig. 3a–c).

We further carried out X-ray absorption spectroscopy (XAS) measurements on *c*-$CoSe_2$ and *o*-$CoSe_2$ catalysts in comparison with *c*-CoS_2 catalyst (Fig. 3d–g). The X-ray absorption near-edge structure (XANES) spectra at Co K-edge (Fig. 3d) matched with previous reports[44, 45] and suggested the identical +2 oxidation state of Co in all three catalysts (whose edge positions coincide and lie in between the Co foil and Co_3O_4 references), and the Se K-edge spectra (Fig. 3e) showed that both $CoSe_2$ polymorphs exhibited the same oxidation state of Se. Extended X-ray absorption fine structure (EXAFS) spectra (Fig. 3f,g) showed that the Co-Se distances in both $CoSe_2$ polymorphs were greater than the Co-S distance in *c*-CoS_2 by ~0.1 Å (see the first shell fitting results in Fig. S8 and Table S2, ESI†), consistent with their lattice constants (Fig. 1a).

Experimental Studies of $CoSe_2$ Polymorphs as Selective $2e^-$ ORR Electrocatalysts

We first used the rotating ring-disk electrode (RRDE) to examine the catalytic activity and selectivity toward electrochemical

H_2O_2 production: the catalyst samples were drop-casted on the glassy carbon disk electrode catalyzing ORR; meanwhile, the surrounding Pt ring electrode was held at a constant potential to selectively oxidize H_2O_2 (the 2e⁻ ORR product) under diffusion-limited conditions without triggering the oxidation of water (the 4e⁻ ORR product). Since ORR depletes protons in the vicinity of the catalyst surface, we checked the local pH near the operating RRDE in O_2-saturated 0.05 M H_2SO_4 solution (pH 1.20) using commercial Pt/C, which catalyzes almost only 4e⁻ ORR, and carbon black, which is moderately selective but poorly active toward 2e⁻ ORR, as benchmark catalysts (Fig. S9, ESI†). We found the local pH was unaffected during electrochemical operations (see Fig. S9 and additional discussion in the ESI†).

We systematically investigated the 2e⁻ ORR activity and selectivity of *c*-$CoSe_2$ and *o*-$CoSe_2$ catalysts to experimentally validate and further elaborate the mechanistic insights predicted by our calculated free energy diagrams and surface Pourbaix diagrams. As these catalyst samples may exhibit different specific surface areas, we performed RRDE measurements of each catalyst with various catalyst loadings for fair comparisons (see Table S3, ESI†). In 0.05 M H_2SO_4 solution (pH 1.20), both $CoSe_2$ polymorph catalysts showed efficient and selective H_2O_2 production at low overpotentials (Fig. 4a), consistent with the calculated free energy diagrams (Fig. 2). The ORR catalytic onset on both $CoSe_2$ polymorphs took place at potentials slightly more positive than the standard equilibrium potential of 2e⁻ ORR (E^o = 0.69 V vs. RHE), which is due to the Nernstian shift in the 2e⁻ ORR equilibrium potential

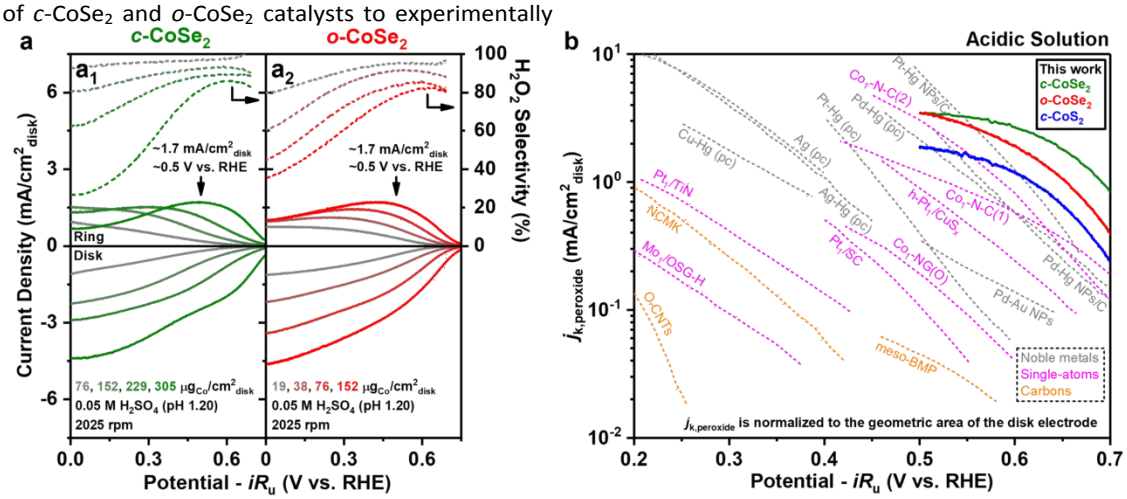

Fig. 4 Electrochemical characterization of selective 2e⁻ ORR on *c*-$CoSe_2$ and *o*-$CoSe_2$ catalysts. (a) RRDE voltammograms recorded at 2025 rpm and the corresponding H_2O_2 selectivity of (a_1) *c*-$CoSe_2$ and (a_2) *o*-$CoSe_2$ catalyst with various catalyst loadings in O_2-saturated 0.05 M H_2SO_4 solution (pH 1.20). (b) Kinetic current densities for H_2O_2 production normalized to the geometric area of the disk electrode ($j_{k,peroxide}$) on *c*-$CoSe_2$ (305 $\mu g_{Co}/cm^2_{disk}$) and *o*-$CoSe_2$ (152 $\mu g_{Co}/cm^2_{disk}$) catalysts, in comparison with *c*-CoS_2 (305 $\mu g_{Co}/cm^2_{disk}$) and previously reported 2e⁻ ORR catalysts (noble metals, single-atom catalysts, and carbon materials) based on RRDE measurements in acidic solution. The traces for *c*-$CoSe_2$, *o*-$CoSe_2$, and *c*-CoS_2 catalysts are from this work, which are recorded at 1600 rpm and cut off at 0.5 V vs. RHE where $j_{peroxide}$ reaches its approximate maximum. Other traces are from previous reports (as summarized in Table S6, ESI†): ref. 26 for Pt-Hg NPs/C and Pt-Hg (pc); ref. 27 for Pd-Hg NPs/C, Pd-Hg (pc), Ag (pc), Ag-Hg (pc), Cu-Hg (pc); ref. 46 for Pd-Au NPs; ref. 47 for Pt_1/SC; ref. 48 for Pt_1/TiN; ref. 49 for h-Pt_1/CuS_x; ref. 19 for Co_1-N-C(1); ref. 21 for Co_1-NG(O); ref. 22 for Co_1-N-C(2); ref. 23 for Mo_1-OSG-H; ref. 13 for O-CNTs; ref. 16 for meso-BMP; ref. 18 for NCMK.

when the bulk concentration of H_2O_2 is very low.[21] We investigated the H_2O_2 selectivity of both $CoSe_2$ polymorphs as a function of overpotential and catalyst loading (Fig. 4a). In the low overpotential region, the overall ORR current density (delivered on the disk electrode) and the partial current density for H_2O_2 production ($j_{peroxide}$, detected on the ring electrode and further adjusted by the collection efficiency) steadily increased with higher catalyst loadings, while the H_2O_2 selectivity appeared to be very high (>80%) and fairly insensitive to the catalyst loading. In the high overpotential region, however, the H_2O_2 production was less selective as the catalyst loading increased. These observations can be rationalized by our calculated surface Pourbaix diagrams (Fig. 1e,f). At low overpotentials, both $CoSe_2$ polymorphs feature high OH* coverages on surface Co sites and fewer unsaturated Co active sites for the undesired OOH* scission, explaining their *intrinsic* high selectivity toward 2e⁻ ORR across various catalyst loadings. As the overpotential increases, both $CoSe_2$ polymorphs form clean surfaces with many unsaturated Co sites, which may allow for the competing 4e⁻ ORR pathway via OOH* scission. As the catalyst loading increases, the total amount of unsaturated Co sites and the catalyst film thickness also increase, which may trigger more side reactions of H_2O_2 reduction and/or decomposition, and lower the H_2O_2 selectivity.[19] These RRDE results suggest that $CoSe_2$ polymorphs should operate at low overpotentials, where they are *intrinsically* selective toward 2e⁻ ORR, and with high catalyst loadings to achieve the optimal overall electrode performances for H_2O_2 production in acidic solution.

We further carried out head-to-head comparisons between both $CoSe_2$ polymorph and CoS_2 catalysts based on RRDE measurements in acidic solution. The catalytic properties of *c*-

CoS_2 and *c*-$CoSe_2$ were directly compared at the same catalyst loading (76, 152, 229, or 305 $\mu g_{Co}/cm^2_{disk}$) because they delivered similar overall current densities (Fig. S10a, ESI†). *c*-$CoSe_2$ was clearly more selective toward 2e⁻ ORR than *c*-CoS_2 in the low overpotential region (Fig. S10a_1–a_4, ESI†), consistent with the calculated surface Pourbaix diagrams which predict that the undesired OOH* scission can be effectively suppressed on $CoSe_2$ due to high OH* coverages on surface Co sites. On the other hand, it was not straightforward to directly compare the catalytic properties of *c*-CoS_2 and *o*-$CoSe_2$ at the same catalyst loading because *o*-$CoSe_2$ delivered a much higher overall ORR current density than *c*-CoS_2 (Fig. S10b_1, ESI†); this is perhaps not surprising given their very different nanoscale morphologies (Fig. 3a). Therefore, we performed fair comparisons between *c*-CoS_2 (76, 152, 229, or 305 $\mu g_{Co}/cm^2_{disk}$) and *o*-$CoSe_2$ (19, 38, 76, or 152 $\mu g_{Co}/cm^2_{disk}$) when they delivered similar overall ORR current densities at different catalyst loadings (Fig. S10b_2–b_5, ESI†). Similar to the *c*-$CoSe_2$ polymorph and as expected from surface Pourbaix diagrams, *o*-$CoSe_2$ was also more selective toward 2e⁻ ORR than *c*-CoS_2 at low overpotentials. Moreover, compared to *c*-CoS_2 and *c*-$CoSe_2$, the H_2O_2 selectivity of *o*-$CoSe_2$ in the high overpotential region was slightly better retained as the catalyst loading increased (Fig. S10, ESI†). Since the binding strength of OH* to *o*-$CoSe_2$ is greater than that to *c*-CoS_2 and *c*-$CoSe_2$, it is less favorable to completely reduce OH* via PCET and form a clean surface of *o*-$CoSe_2$ at high overpotentials, which may result in its enhanced H_2O_2 selectivity in the high overpotential region.

These RRDE experiments confirm that both $CoSe_2$ polymorphs are highly active and selective 2e⁻ ORR electrocatalysts in acidic solution. The optimal overall electrode performances for H_2O_2 production can be achieved at the highest catalyst loadings when $j_{peroxide}$ reached the maximum of ~1.7 mA/cm^2_{disk} at ~0.5 V vs. RHE on both catalysts (Fig. 4a), but *o*-$CoSe_2$ required a much lower catalyst loading (152 $\mu g_{Co}/cm^2_{disk}$) than *c*-$CoSe_2$ (305 $\mu g_{Co}/cm^2_{disk}$) to achieve a similar overall electrode performance, because the *o*-$CoSe_2$ sample exhibited a much higher double layer capacitance (C_{dl}) value and thus a larger electrochemically active surface area (ECSA) than the *c*-$CoSe_2$ sample (Fig. S11 and Table S4, ESI†). Therefore, the high-surface-area *o*-$CoSe_2$ catalyst is more advantageous for practical electrochemical H_2O_2 production because of the lower catalyst loadings and reduced catalyst cost.

To quantitatively compare the H_2O_2 production performances of both $CoSe_2$ catalysts with previously reported 2e⁻ ORR catalysts in acidic solution, we extracted *kinetic* current density for H_2O_2 production ($j_{k,peroxide}$) by correcting as-measured $j_{peroxide}$ for mass-transport loss using Koutecky-Levich (K-L) analysis based on RRDE voltammograms recorded at various rotation rates. An example of the K-L analysis on *c*-$CoSe_2$ catalyst is shown in Fig. S12 and Table S5 (ESI†). $j_{k,peroxide}$ is normalized the geometric area of the disk electrode to reflect *the overall yield* of H_2O_2 product without mass-transport limitation, which clearly increased with higher catalyst loadings (Fig. S12c, ESI†). Although this $j_{k,peroxide}$ normalized to the disk area can be affected by the catalyst loading and the catalyst surface area and thus does not reflect the intrinsic catalyst property, it is important for practical applications. Therefore, we chose the highest catalyst loadings of *c*-$CoSe_2$ (305 $\mu g_{Co}/cm^2_{disk}$) and *o*-$CoSe_2$ (152 $\mu g_{Co}/cm^2_{disk}$) for comparisons with previously reported 2e⁻ ORR catalysts in acidic solution (Fig. 4b). Both *c*-$CoSe_2$ and *o*-$CoSe_2$ catalysts show clearly more efficient H_2O_2 production than *c*-CoS_2 and other reported single-atom[22] or carbon[18] catalysts, and display even better overall electrode performances than the state-of-the-art noble metal catalysts[26, 27] in the more important low overpotential region. This comparison of $j_{k,peroxide}$ reveals that $CoSe_2$ polymorph catalysts are the best-performing 2e⁻ ORR electrocatalysts reported so far in *acidic* solution (as summarized in Table S6, ESI†).

Enhanced Catalyst Stability of $CoSe_2$ Polymorphs from RRDE Measurements

We examined the catalyst stability of both $CoSe_2$ polymorphs for electrochemical H_2O_2 production in 0.05 M H_2SO_4 solution by continuously applying RRDE scans while sequentially changing the rotation rate (Fig. S13a, ESI†), analogous to the accelerated degradation tests typically applied to conventional 4e⁻ ORR catalysts.[50, 51] These RRDE scans recorded at the highest rotation rate of 2025 rpm clearly revealed the enhanced catalyst stability of *c*-$CoSe_2$ (305 $\mu g_{Co}/cm^2_{disk}$) and *o*-$CoSe_2$ (152 $\mu g_{Co}/cm^2_{disk}$) (Fig. 5a). The disk currents and the ring currents of both $CoSe_2$ polymorphs were relatively stable during catalyst stability tests (Fig. 5a_2,a_3), whereas those of *c*-CoS_2 (305 $\mu g_{Co}/cm^2_{disk}$) evidently decreased over time (Fig. 5a_1). We

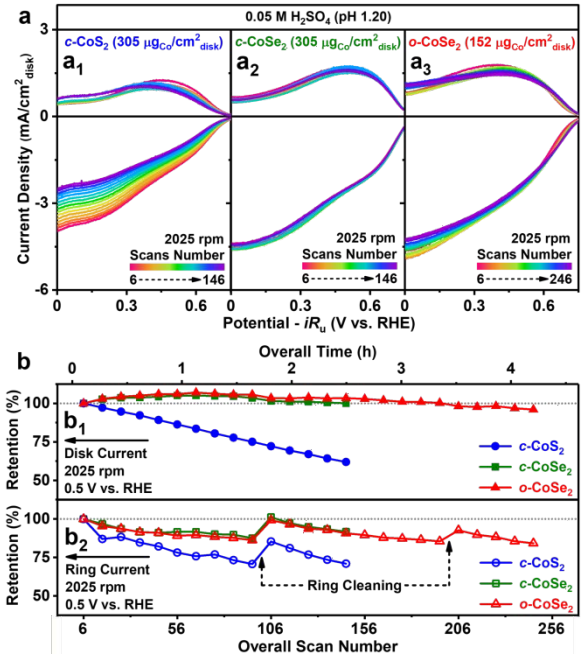

Fig. 5 Enhanced stability of *c*-$CoSe_2$ and *o*-$CoSe_2$ catalysts from RRDE measurements. (a) RRDE voltammograms of (a_1) *c*-CoS_2 (305 $\mu g_{Co}/cm^2_{disk}$), (a_2) *c*-$CoSe_2$ (305 $\mu g_{Co}/cm^2_{disk}$), and (a_3) *o*-$CoSe_2$ (152 $\mu g_{Co}/cm^2_{disk}$) recorded at 2025 rpm during catalyst stability tests in O_2-saturated 0.05 M H_2SO_4 solution (pH 1.20). (b) Retention rates of (b_1) disk current and (b_2) ring current at 2025 rpm and 0.5 V vs. RHE (where $j_{peroxide}$ reaches its approximate maximum) during catalyst stability tests. The rotation rate profile of catalyst stability tests and the protocol for electrochemical cleaning of the ring electrode are shown in Fig. S13 (ESI†).

further quantitatively compared the disk current and ring current retentions of all three catalysts at 0.5 V vs. RHE where $j_{peroxide}$ reached its approximate maximum (Fig. 5b). Over the same time period of 2.5 h, the disk current of *c*-$CoSe_2$ was almost completely retained (~100%), whereas *c*-CoS_2 only retained 62% of its initial disk current (Fig. 5b$_1$). Notably, the high-surface-area *o*-$CoSe_2$ displayed a near-unity disk current retention over a longer time period of 4.2 h (Fig. 5b$_1$). Note that the slight decrease in the ring currents of both $CoSe_2$ polymorphs (Fig. 5b$_2$) was mainly due to the formation of surface PtO_x on the ring electrode after its continuous operation at the high potential of 1.3 V vs. RHE.[13, 20] After periodic electrochemical cleaning of the ring electrode (see Fig. S13b, ESI†, for details), the ring currents of both $CoSe_2$ polymorphs were immediately recovered (Fig. 5b$_2$), indicating that the electrochemical H_2O_2 production was stable on both $CoSe_2$ polymorphs.

consistent with our theoretical prediction that both $CoSe_2$ polymorphs are better resistant to surface oxidation than *c*-CoS_2, because the binding strength of O* to Se sites is substantially weaker than that to S sites by 0.59 eV, and display significantly enhanced catalyst stability for the electrosynthesis of H_2O_2 in acidic solution.

Bulk Electrosynthesis and Chemical Detection of H_2O_2 Produced on $CoSe_2$ Marcasite

From a practical perspective, it is critical to confirm that the electrogenerated H_2O_2 on $CoSe_2$ catalysts can indeed accumulate in solution and reach concentrations that are relevant to applications, for example, no more than 1000 ppm (29 mM) for water treatment.[4] RRDE measurements only allow instantaneous and *electrochemical* detection of H_2O_2. Therefore, we performed bulk electrolysis to produce H_2O_2 using integrated electrode of *o*-$CoSe_2$ nanowires directly grown

Table 1 Average cobalt leaching rates of *c*-$CoSe_2$ and *o*-$CoSe_2$ in comparison with *c*-CoS_2 during catalyst stability tests in 0.05 M H_2SO_4 solution from RRDE measurements.

Catalyst	Catalyst Loading[a]	Stability Test Duration	[Co] in Tested Electrolyte[b]	Average Cobalt Leaching Rate
c-CoS_2	305 $\mu g_{Co}/cm^2_{disk}$	2.5 h (151 scans)	36.6 $\mu g_{Co}/L$	0.66 $\mu g_{Co}/h$
c-$CoSe_2$	305 $\mu g_{Co}/cm^2_{disk}$	2.5 h (151 scans)	21.8 $\mu g_{Co}/L$	0.39 $\mu g_{Co}/h$
o-$CoSe_2$	152 $\mu g_{Co}/cm^2_{disk}$	4.2 h (251 scans)	28.5 $\mu g_{Co}/L$	0.31 $\mu g_{Co}/h$

[a]Geometric area of the disk electrode is 0.126 cm^2_{disk}.

[b][Co] in the tested electrolyte solution (45 mL) was determined by ICP-MS analysis (see details in Table S8, ESI†).

To better understand the origin of the enhanced catalyst stability of $CoSe_2$, we recovered all of the tested catalysts to examine their surface composition and structural integrity using Raman spectroscopy and XPS. Raman spectra suggested the crystal structures of all tested catalysts, including the apparently least stable *c*-CoS_2 catalyst, were well retained without the formation of crystalline or amorphous impurities (Fig. S14, ESI†). XPS spectra suggested their surface chemical states remained the same as the pristine catalysts (Fig. S15, ESI†). This is understandable because the bulk Pourbaix diagram (Fig. S1a, ESI†) suggests the degradation of *c*-CoS_2 via surface oxidation yields soluble species of Co^{2+} and SO_4^{2-} that can readily leach into electrolyte solutions without being detected by XPS. The leaching of *c*-CoS_2 was also implied by the slight change in its surface composition after the catalyst stability test, whereas both $CoSe_2$ polymorphs appeared to be more stable with minimal changes in their surface compositions (Table S7, ESI†). Therefore, it is essential to quantify the Co^{2+} leaching rate by using inductively coupled plasma mass spectrometry (ICP-MS) to analyze the tested electrolyte solutions, so that the stability of these three catalysts can be differentiated based on the total amount of Co^{2+} leached per hour ($\mu g_{Co}/h$). As summarized in Table 1 (also see details in Table S8, ESI†), the more stable *o*-$CoSe_2$ (152 $\mu g_{Co}/cm^2_{disk}$) and *c*-$CoSe_2$ (305 $\mu g_{Co}/cm^2_{disk}$) exhibited similar leaching rates of 0.31 and 0.39 $\mu g_{Co}/h$, respectively, whereas the least stable *c*-CoS_2 (305 $\mu g_{Co}/cm^2_{disk}$) leached almost twice as fast (0.66 $\mu g_{Co}/h$). In fact, this Co^{2+} leaching from $CoSe_2$ could potentially be transient and take place mostly at the initial stage of electrochemical operations (see later discussion). These leaching results are

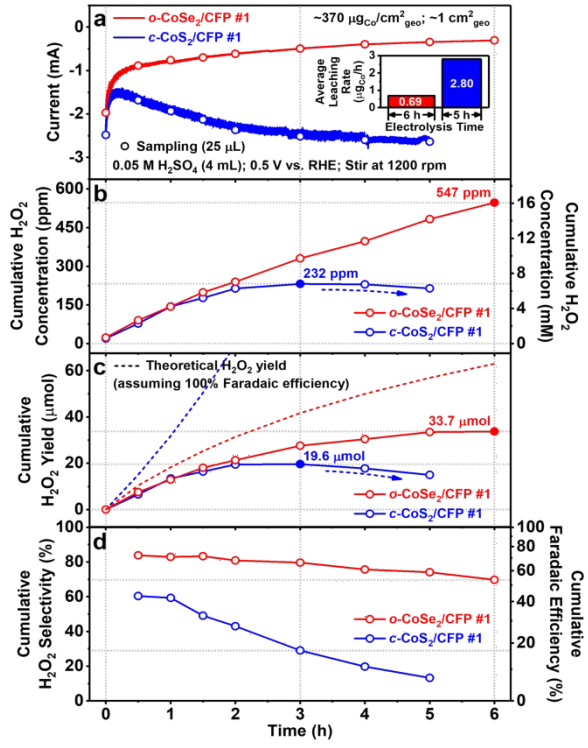

Fig. 6 Bulk electrosynthesis and chemical detection of H_2O_2 produced on *o*-$CoSe_2$/CFP in comparison with *c*-CoS_2/CFP. (a) Chronoamperometry curves of *o*-$CoSe_2$/CFP and *c*-CoS_2/CFP (with the same catalyst loading of ~370 $\mu g_{Co}/cm^2_{geo}$ and the same geometric area of ~1 cm^2_{geo}) at 0.5 V vs. RHE in O_2-saturated 0.05 M H_2SO_4 solution (pH 1.20) under vigorous stirring (1200 rpm). The average cobalt leaching rates ($\mu g_{Co}/h$) of *o*-$CoSe_2$/CFP and *c*-CoS_2/CFP during bulk electrolysis is shown as an inset. (b) Cumulative H_2O_2 concentration, (c) cumulative H_2O_2 yield, and (d) cumulative H_2O_2 selectivity and Faradaic efficiency during bulk electrolysis.

on three-dimensional carbon fiber paper substrate (denoted as *o*-$CoSe_2$/CFP, see Fig. S16, ESI†) and carried out *chemical* detection of the produced H_2O_2 via redox titration using cerium(IV) sulfate ($2\ Ce^{4+} + H_2O_2 \rightarrow 2\ Ce^{3+} + 2\ H^+ + O_2$) followed by UV-Vis spectrophotometry.[13] We chose *o*-$CoSe_2$ (marcasite) over *c*-$CoSe_2$ (pyrite) for bulk electrolysis experiments because our earlier RRDE results showed that *o*-$CoSe_2$ featured a higher C_{dl} value (which implies a larger ECSA) and delivered a higher catalytic current for H_2O_2 production than *c*-$CoSe_2$ at the same catalyst loading (Fig. 4a). For comparison purposes, another working electrode of *c*-CoS_2 nanowires grown on carbon fiber paper (*c*-CoS_2/CFP, see Fig. S17, ESI†) that had the same geometric area of ~1 cm^2_{geo} (Fig. S19, ESI†) and same catalyst loading of ~370 $\mu g_{Co}/cm^2_{geo}$ (Table S9, ESI†) was studied. Bulk electrosynthesis of H_2O_2 was performed in a two-compartment three-electrode H-cell setup (Fig. S18, ESI†, also see details in the Experimental Section).

We carried out the bulk electrosynthesis of H_2O_2 on *o*-$CoSe_2$/CFP and *c*-CoS_2/CFP in O_2-saturated 0.05 M H_2SO_4 solution (4 mL) at the constant potential of 0.5 V vs. RHE, near the optimal potential where the maximum $j_{peroxide}$ was achieved from RRDE measurements, over long periods of time (5–6 h, see Fig. 6). As the H_2O_2 product was accumulated in the solution, the overall catalytic current of *o*-$CoSe_2$/CFP displayed a Nernstian response (Fig. 6a red curve). In contrast, the overall catalytic current of *c*-CoS_2/CFP only exhibited an initial Nernstian response immediately after the bulk electrolysis started and then gradually *increased* as the bulk electrolysis proceeded (Fig. 6a blue curve). The produced H_2O_2 was periodically quantified at various time points using the UV-vis spectrophotometric method described above (Fig. S22, ESI†, also see details in the Experimental Section). During the bulk electrolysis using *o*-$CoSe_2$/CFP, the cumulative H_2O_2 concentration kept increasing and reached a high concentration of 547 ppm after 6 h (Fig. 6b red curve). As for *c*-CoS_2/CFP, despite delivering a larger overall catalytic current, the cumulative H_2O_2 concentration increased less steadily and only reached a maximum of 232 ppm over 3 h and then started decreasing afterwards (Fig. 6b blue curve). We further calculated the cumulative H_2O_2 yield on both electrodes taking into account the evaporation of electrolyte solution during bulk electrolysis (see Table S10, ESI†, for details): the cumulative H_2O_2 yield on *o*-$CoSe_2$/CFP with only 19.6 μmol (Fig. 6c). As a result, the cumulative H_2O_2 selectivity on *o*-$CoSe_2$/CFP reached ~83% during the first hour of bulk electrolysis and still remained ~70% over the long period of 6 h, whereas the selectivity on *c*-CoS_2/CFP started off with a lower value of ~60% and drastically decreased to ~13% over 5 h (see Fig. 6d and Table S11, ESI†). Moreover, ICP-MS analysis of the tested electrolyte solutions (see Table S12, ESI†, and inset of Fig. 6a) showed that *o*-$CoSe_2$/CFP exhibited an average cobalt leaching rate of 0.69 μg_{Co}/h over 6 h, much lower than that of *c*-CoS_2/CFP (2.80 μg_{Co}/h over 5 h). In fact, since the Co^{2+} leaching from $CoSe_2$ took place mostly at the initial stage of electrochemical operations (see later discussion), this average leaching rate of 0.69 μg_{Co}/h could be a *lower bound* estimate of the operational stability of *o*-$CoSe_2$/CFP. These observations also led us to suspect that *electrochemical* side reactions of H_2O_2 reduction and/or decomposition were much more pronounced on *c*-CoS_2/CFP and eventually outcompeted the H_2O_2 production, which could account for the abnormal increase in the overall current (Fig. 6a) and the significant decrease in the H_2O_2 selectivity (Fig. 6d) during the bulk electrolysis using *c*-CoS_2/CFP.

We designed additional bulk electrolysis experiments to prove that the *electrochemical* side reactions of H_2O_2 reduction and/or decomposition are indeed much less prone on *o*-$CoSe_2$/CFP. We reason that the additional catalytic current triggered by those side reactions should correlate with the H_2O_2 concentration. Therefore, after accumulating an appreciable concentration of H_2O_2 from the bulk electrolysis using *o*-$CoSe_2$/CFP, we reintroduced fresh *H_2O_2-free* electrolyte solution and performed another bulk electrolysis reusing the same *o*-$CoSe_2$/CFP electrode (Fig. S21a–d, ESI†). The overall catalytic current of *o*-$CoSe_2$/CFP in the H_2O_2-free solution was identical to that in the H_2O_2-containing solution (Fig. S21a, ESI†), suggesting *o*-$CoSe_2$/CFP is highly resistant to those electrochemical side reactions that consume the H_2O_2 product. In contrast, *c*-CoS_2/CFP behaved very differently in the analogous experiments (Fig. S21e–h, ESI†). The overall catalytic current of *c*-CoS_2/CFP in the H_2O_2-containing solution was substantially greater than that in the fresh H_2O_2-free solution (Fig. S21e, ESI†), resulting in the significant loss of H_2O_2 product due to the prevalence of side reactions. Therefore, *o*-$CoSe_2$/CFP is much more effective than *c*-CoS_2/CFP for the bulk electrosynthesis of H_2O_2 that can reach practically useful concentrations.

We further utilized these bulk electrolysis experiments to investigate the catalyst leaching behaviors of *o*-$CoSe_2$/CFP vs. *c*-CoS_2/CFP in more details. We collected the tested electrolyte solutions at the end of each consecutive run of bulk electrolysis using each working electrode (Fig. S21, ESI†) and performed ICP-MS analysis to examine the cobalt leaching rate during each run (Fig. S22, also see Table S12 and S13, ESI†). We observed *transient* leaching of *o*-$CoSe_2$/CFP taking place mostly at the initial stage of electrochemical operations, and the Co^{2+} leaching was negligible during the second run of bulk electrolysis (see Fig. S22a,b, ESI†, for two replicate experiments). This transient leaching could be due to the loss of loosely-bound *o*-$CoSe_2$ particles from CFP substrate at the beginning. In fact, if this initial transient leaching was excluded, the cobalt leaching rate of *o*-$CoSe_2$/CFP after reaching its steady state was less than 0.2 μg_{Co}/h (Fig. S22a,b, ESI†). In contrast, *c*-CoS_2/CFP displayed *continuous* leaching behavior during both runs of bulk electrolysis (Fig. S22c, ESI†) with a leaching rate greater than 2 μg_{Co}/h, an order of magnitude higher than *o*-$CoSe_2$/CFP. These *bulk* leaching results further confirmed the enhanced electrochemical stability of *o*-$CoSe_2$ under more stringent operating conditions for a much longer timescale. To our knowledge, there has been no rigorous analysis of metal leaching in the recently reported earth-abundant $2e^-$ ORR catalysts for a direct comparison, but we found that the steady state cobalt leaching rate of *o*-$CoSe_2$ presented here is much lower than those of other cobalt-based electrocatalysts recently reported for water splitting reactions (Table S14, ESI†).

Hopefully this careful study on the stability of earth-abundant 2e⁻ ORR catalysts through quantitative metal leaching rate analysis will stimulate the research community to look into this important issue more in the future. Furthermore, Raman, XPS (Fig. S23 and Table S7, ESI†), and XAS (Fig. S24 and Table S15, ESI†) characterization confirmed the structural and compositional integrity of the tested *o*-$CoSe_2$/CFP electrodes after the bulk electrosynthesis of H_2O_2.

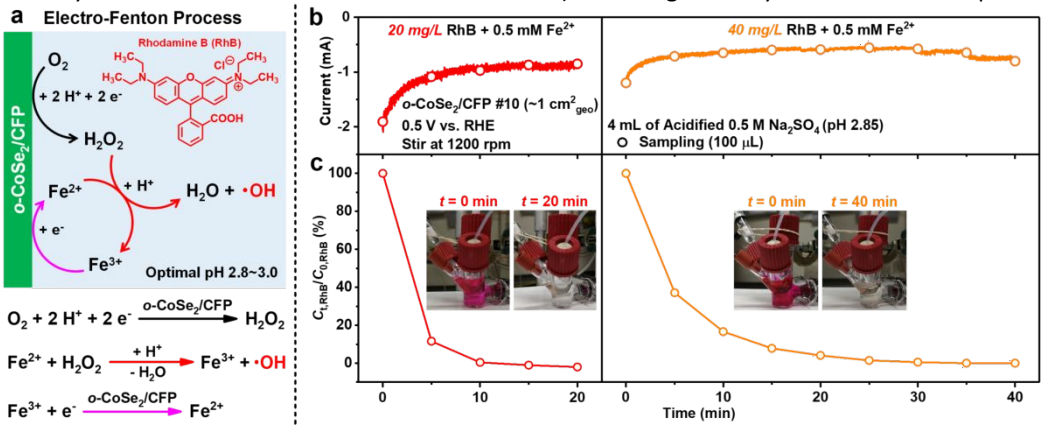

Fig. 7 Electro-Fenton degradation of Rhodamine B (RhB) on *o*-$CoSe_2$/CFP. (a) Schematic of the electro-Fenton process and the (electro)chemical reactions involved. (b) Chronoamperometry curves of *o*-$CoSe_2$/CFP at 0.5 V vs. RHE when both RhB and Fe^{2+} are present in O_2-saturated acidified 0.5 M Na_2SO_4 solution (pH 2.85) under vigorous stirring (1200 rpm) at room temperature. The same *o*-$CoSe_2$/CFP cathode is reused for two consecutive electro-Fenton degradation tests with different initial concentrations of RhB (20 or 40 mg/L) but the same concentration of Fe^{2+} (0.5 mM). (c) Decays of the RhB concentrations over time. The inset photographs show the color changes of the electrolyte solutions before and after each electro-Fenton degradation test.

Significantly, the accumulated concentration of 547 ppm H_2O_2 using *o*-$CoSe_2$/CFP demonstrated here is the highest among the few previous reports of 2e⁻ ORR electrocatalysts that showed the bulk electrosynthesis of H_2O_2 in *acidic* solution in similar H-cells (see Table S16 and additional discussion in the ESI†).[22, 26] In fact, the cumulative H_2O_2 concentrations previously demonstrated were one or two order(s) of magnitude lower because larger volumes of electrolyte solution was often used. The stable operation of *o*-$CoSe_2$/CFP for 6 h demonstrated here is among the longest trial of the bulk electrosynthesis of H_2O_2 in *acidic* solution and, more importantly, *no* other report ever examined the catalyst leaching under these practically relevant conditions (Table S16, ESI†). Given the insights discussed above on the possible electrochemical side reactions of H_2O_2 at higher H_2O_2 concentrations, the catalyst stability is less challenged when evaluated under much less stringent operating conditions without a significant buildup of H_2O_2 in the electrolyte solution. To accumulate a high concentration of H_2O_2 useful for practical applications, we not only need highly active and selective 2e⁻ ORR electrocatalysts, they also must be robust and highly resistant to electrochemical side reactions under stringent operating conditions.

Electro-Fenton Degradation of Model Organic Pollutant on $CoSe_2$ Marcasite

H_2O_2 is particularly useful for water treatment and environmental remediation, utilizing the Fenton's reaction between H_2O_2 and Fe^{2+} (Equation 10) to generate hydroxyl radical (·OH) as an even more powerful oxidant ($E^{o}_{\cdot OH/H_2O}$ = 2.80 V vs. SHE). This approach can be used to remove persistent organic pollutants[52-54] from wastewater through advanced oxidation processes. Furthermore, in the so-called *electro*-Fenton process, H_2O_2 is electrogenerated from 2e⁻ ORR at the cathode, while Fe^{2+} is rapidly regenerated from the reduction of Fe^{3+} (E^{o} = 0.77 V vs. SHE, Equation 11) at the same cathode (Fig. 7a).[24] This significantly enhances the ·OH production rates and the organics mineralization capabilities compared to the conventional *chemical* Fenton process.[25] It is noteworthy that the Fenton's reaction exhibits the highest rate at an optimal acidic pH of 2.8–3.0 when the speciation of Fe^{2+} reaches its maximum.[24] Therefore, the successful bulk electrosynthesis of H_2O_2 in *acidic* solution makes *o*-$CoSe_2$/CFP a promising cathode for the electro-Fenton process.

$$Fe^{2+} + H_2O_2 + H^+ \rightarrow Fe^{3+} + H_2O + \cdot OH \quad (10)$$

$$Fe^{3+} + e^- \rightarrow Fe^{2+} \quad (11)$$

We used Rhodamine B (RhB) as a model organic pollutant[55] to demonstrate the effective electro-Fenton process on *o*-$CoSe_2$/CFP (Fig. 7a). Electro-Fenton degradation tests were performed at room temperature in O_2-saturated acidified 0.5 M Na_2SO_4 solution (pH 2.85) with the presence of both RhB (20 or 40 mg/L) and Fe^{2+} (0.5 mM) in a three-electrode H-cell setup using *o*-$CoSe_2$/CFP as the working cathode operated at 0.5 V vs. RHE (same as the earlier bulk electrolysis experiments) to enable efficient H_2O_2 production. We used UV-Vis spectrophotometry to monitor the organic dye concentration as a function of time during each test (Fig. S25, ESI†). The overall catalytic current of the *o*-$CoSe_2$/CFP cathode displayed a Nernstian response, indicating the accumulation of the electrogenerated H_2O_2 in solution (Fig. 7b). During the same time, the concentration of RhB decreased rapidly (Fig. 7c) and the color of the solutions faded (insets of Fig. 7c). Moreover, this current remained steady regardless of the decay of the RhB concentration over time (Fig. 7b,c), suggesting that RhB was degraded via the electro-Fenton process rather than the direct electrochemical destruction on the cathode. Significantly, the *o*-

$CoSe_2$/CFP cathode completely degraded and decolored 20 mg/L of RhB within a short period of 20 min, and remained highly efficient when it was reused for removing higher concentrations (40 mg/L) of RhB under similar operating conditions (Fig. 7c). These results show that *o*-$CoSe_2$ is a very promising cathode for electro-Fenton process and water treatment applications, which is rooted in its enhanced selectivity and stability for the bulk electrosynthesis of H_2O_2 in *acidic* solution.

Conclusions

In conclusion, this joint computational/experimental study demonstrates stable and selective electrosynthesis of H_2O_2 and effective electro-Fenton process on $CoSe_2$ polymorph catalysts in acidic solution, establishing new understandings on catalyst stability for $2e^-$ ORR and significantly advancing the practical production and utilization of H_2O_2 in acidic solution. Calculated surface Pourbaix diagrams reveal the weak binding of O* to Se sites and predict better electrochemical stability for $CoSe_2$ than CoS_2. Additionally, both $CoSe_2$ polymorphs are computationally predicted to be active and selective $2e^-$ ORR electrocatalysts. RRDE experiments in 0.05 M H_2SO_4 show that $CoSe_2$ polymorphs are the best-performing $2e^-$ ORR electrocatalysts reported so far in *acidic* solution, delivering higher kinetic current densities for H_2O_2 production at low overpotentials than reported state-of-the-art noble metal or single-atom catalysts. Detailed structural characterization and ICP-MS analysis of tested $CoSe_2$ catalysts and electrolyte solutions confirm their enhanced catalyst stability and resistance to catalyst leaching during prolonged electrochemical operations. Using *o*-$CoSe_2$ nanostructures directly grown on carbon fiber paper electrode, bulk electrosynthesis of H_2O_2 in 0.05 M H_2SO_4 achieved a high accumulated H_2O_2 concentration of 547 ppm (16 mM) thanks to the effective suppression of electrochemical side reactions, surpassing other reported $2e^-$ ORR catalysts evaluated in *acidic* solution in similar H-cells. Such robust H_2O_2 production allows for the effective electro-Fenton process on the *o*-$CoSe_2$ electrode and the efficient degradation of a model organic pollutant, demonstrating its great promise for on-site water treatment applications. This integrated study not only establishes $CoSe_2$ polymorphs as the new benchmark $2e^-$ ORR electrocatalysts in *acidic* solution and demonstrates effective on-site electrosynthesis of H_2O_2, but also reveals new mechanistic insights and introduces new design rules for stable and efficient earth-abundant transition metal compound electrocatalysts for decentralized production and utilization of H_2O_2.

Experimental Section

Computational Method

Spin polarized electronic structure calculations were performed using the Vienna Ab initio Simulation package (VASP)[56-59] interfaced with the Atomic Simulation Environment (ASE).[60] Projector augmented wave (PAW) pseudopotentials[61, 62] with a cutoff of 450 eV were used to treat core electrons, and the Perdew-Burke-Ernzerhof (PBE) functional[63, 64] was used to treat exchange and correlation. Dispersion was treated using Grimme's D3(ABC) method.[65] To better describe the Co 3d electrons in *c*-$CoSe_2$, a Hubbard U parameter,[66] U_{eff} = 2.0 eV, was taken from a previous report.[67] A variety of Hubbard U parameters were tested for *c*-CoS_2 and *o*-$CoSe_2$, and were found to have little to no effect on geometries or energies; therefore, no Hubbard U parameter was used for these two catalysts. Solvation effects were treated using the continuum solvent method VASPsol.[68, 69] The Brillouin zone was sampled using a (10,10,10) and (10,10,1) Γ-centered Monkhorst-Pack mesh[70] for bulk and surface calculations, respectively. Lattice constants were determined by fitting to an equation of state (EOS).[71] The (100) surfaces of *c*-CoS_2 and *c*-$CoSe_2$ and (101) surface of *o*-$CoSe_2$ were modelled as a 1×1 unit cell slab with two repeats in the z-direction, leading to a total of 8 Co atoms and 16 S/Se atoms and a vacuum gap of at least 15 Å. The top half of the slabs were allowed to relax while the bottom half were frozen to simulate bulk. For each ionic configuration, the electronic energy was converged below 10^{-6} eV. Both the clean slab and adsorbates were allowed to relax until forces were converged below 0.005 eV/Å^2. Transition states were located using the nudged elastic band (NEB) method[72, 73] and were refined using the dimer method.[74-76] All transition states were confirmed saddle points with one imaginary frequency corresponding to bond breaking. Binding energies were calculated with respect to $O_{2(g)}$ and $H^+_{(aq)}$ and e^-. The energy of $H^+_{(aq)}$ and e^- was calculated using the computational hydrogen electrode (CHE) method,[39] where $H^+_{(aq)}$ is assumed to be in thermodynamic equilibrium with $H_{2(g)}$. In order to avoid well-known errors in the DFT treatment of $O_{2(g)}$, the free energy of $O_{2(g)}$ was determined by matching the experimental standard equilibrium potential (1.229 V) of the reaction $½\ O_{2(g)} + 2\ H^+_{(aq)} + 2\ e^- \rightarrow H_2O_{(l)}$. The free energies of species were calculated using G = H – T S, where H is the enthalpy including zero-point energy (ZPE) and thermal corrections, and S is either the total experimental entropy at 298 K and 1 bar (for gas phase species) or calculated under the harmonic approximation (for surface bound species). The free energy of $H_2O_{(l)}$ was calculated using the experimental free energy of formation for $H_2O_{(l)}$ and $H_2O_{(g)}$. The solvation free energy of $H_2O_{2(aq)}$ was calculated using the experimental Henry's law constant.[77] The calculated standard equilibrium potential of 2e- ORR reaction $O_{2(g)} + 2\ H^+_{(aq)} + 2\ e^- \rightarrow H_2O_{2(aq)}$ is 0.81 V, while the experimental standard equilibrium potential is 0.69 V.

Chemicals

All chemicals were purchased from Sigma-Aldrich and used as received without further purification, unless noted otherwise. Deionized nanopure water (18.2 MΩ·cm) from Thermo Scientific Barnstead water purification systems was used for all experiments.

Materials Synthesis

The synthesis of nanostructured *c*-$CoSe_2$, *o*-$CoSe_2$, and *c*-CoS_2 catalysts as well as the direct growth of *o*-$CoSe_2$ and *c*-CoS_2

nanowires on carbon fiber paper substrates (*o*-$CoSe_2$/CFP and *c*-CoS_2/CFP) followed published procedures[31, 43] with minor modifications. Detailed methods are described in the ESI†.

Materials Characterization

Powder X-ray diffraction (PXRD) patterns were collected on a Bruker D8 ADVANCE powder X-ray diffractometer using Cu Kα radiation. Scanning electron microscopy (SEM) was performed on a Zeiss SUPRA 55VP field emission scanning electron microscope at the accelerating voltage of 1 kV. X-ray photoelectron spectroscopy (XPS) was performed on a Thermo Scientific K-Alpha XPS system with an Al Kα X-ray source. Raman spectroscopy was collected on a Horiba LabRAM ARAMIS Raman spectrometer using a 532 nm laser source with an attenuated laser intensity to avoid sample degradation. X-ray absorption spectroscopy (XAS) was collected in the transmission mode at the Advanced Photon Source (APS) Beamline 10-BM-B, and was analyzed using ATHENA and ARTEMIS softwares.[78] Detailed sample preparation are described in the ESI†.

Electrode Preparation

Drop-casted catalyst powders were prepared on a rotating ring-disk electrode (RRDE-3A, ALS Co., Ltd) made of a glassy carbon disk (with a geometric area of 0.126 cm^2) surrounded by a Pt ring. The collection efficiency of the bare RRDE was 0.43 based on experimental calibration using ferri-/ferrocyanide redox couple. The RRDE was polished with 1, 0.3, and 0.05 μm alumina suspensions (Allied High Tech Products) on a polishing cloth (Buehler, MicroCloth) successively, thoroughly rinsed with nanopure water and methanol, briefly sonicated in methanol for less than 20 s, and dried under ambient condition before use. Catalyst inks were prepared by suspending pre-weighed catalyst powders in desired volumes of the 9:1 (v/v) mixture of nanopure water and 5 wt% Nafion solution via sonication for 1 h. A fixed volume of catalyst ink was then drop-casted onto the glassy carbon disk and dried under ambient condition at the rotation rate of 700 rpm to form a uniform catalyst film with controlled catalyst loading (see Table S3, ESI†).

Electrochemical Measurements

RRDE measurements were conducted in an undivided three-electrode cell using a Bio-Logic VMP-300 multichannel potentiostat. A graphite rod and a Hg/Hg_2SO_4 (saturated K_2SO_4) electrode was used as the counter electrode and the reference electrode, respectively. The acidic electrolyte solution of 0.05 M H_2SO_4 (pH 1.20) was prepared from concentrated H_2SO_4 (95.0–98.0%). The Hg/Hg_2SO_4 reference electrode was calibrated against a standard saturated calomel electrode (SCE, E_{SCE} = 0.241 V vs. SHE):

$$E_{Hg/Hg_2SO_4} = E_{SCE} + 0.403 \text{ V vs. SCE} = 0.644 \text{ V vs. SHE}$$

All potentials were reported versus reversible hydrogen electrode (RHE): E vs. RHE = E vs. SHE + 0.059 V × pH = E vs. Hg/Hg_2SO_4 + 0.715 V. Prior to RRDE measurements, the electrolyte solution was purged with O_2 gas for at least 15 min. During the measurements, a blanket of O_2 gas was maintained over the surface of the electrolyte solution. Under O_2-saturated condition, the Pt ring was first conditioned by running cyclic voltammetry (CV) between 0.05 and 1.20 V vs. RHE (without *iR*-correction) at 100 mV/s and 1600 rpm for 10 cycles, meanwhile holding the disk at 0.75 V vs. RHE; the catalyst-coated disk was then conditioned by running CV between -0.025 and 0.75 V vs. RHE (without *iR*-correction) at 100 mV/s and 1600 rpm for 10 cycles, meanwhile holding the Pt ring at 1.3 V vs. RHE. The catalytic properties were evaluated by performing linear sweep voltammetry (LSV) of the catalyst-coated disk from 0.75 to -0.025 V vs. RHE (without *iR*-correction) at 50 mV/s and various rotation rates, meanwhile holding the Pt ring at 1.3 V vs. RHE. The electrolyte solution was finally saturated with Ar gas for background current measurements. Uncompensated resistance (R_u) was measured by electrochemical impedance spectroscopy (EIS), *iR*-correction was manually performed after background current correction. The H_2O_2 selectivity (p) is calculated using the following equation:

$$p = \frac{2 \times \frac{i_{ring}}{N}}{i_{disk} + \frac{i_{ring}}{N}} \times 100\%$$

where i_{disk} and i_{ring} are the background-corrected disk and ring current, respectively, N is the collection efficiency (0.43). For the ease of directly visualizing the H_2O_2 selectivity from RRDE voltammograms, both the disk and the ring current densities (j_{disk} and j_{ring}) are normalized to the geometric area of the disk electrode (A_{disk}), and the ring current density is further adjusted by the collection efficiency:

$$j_{disk} = \frac{i_{disk}}{A_{disk}}$$

$$j_{ring} = \frac{i_{ring}}{A_{disk} \times N} = j_{peroxide}$$

where $j_{peroxide}$ is the partial disk current density for H_2O_2 production. Detailed derivation of the kinetic current density for H_2O_2 production ($j_{k,peroxide}$) from Koutecky-Levich analysis of $j_{peroxide}$ is described in the ESI†. To estimate electrochemically active surface area (ECSA), double layer capacitance (C_{dl}) was determined under Ar-saturated condition by performing CV of the catalyst-coated disk between -0.025 V and 0.75 V vs. RHE (without *iR*-correction) at various scan rates. After RRDE measurements, the tested electrolyte solutions were collected and filtered with 0.22 μm syringe filters (Restek) three times, then the concentrations of the dissolved Co^{2+} were measured by inductively coupled plasma mass spectrometry (ICP-MS) using a Shimadzu ICPMS-2030 spectrometer. ICP-MS standard solutions were prepared by dissolving $CoSO_4 \cdot 7H_2O$ (≥99%) in a solution of 0.05 M H_2SO_4.

Bulk Electrosynthesis and Chemical Detection of the Produced H_2O_2

o-$CoSe_2$/CFP and *c*-CoS_2/CFP (both with the area of ~1 cm^2_{geo} and the catalyst loading of ~370 $\mu g_{Co}/cm^2_{geo}$) were used as the working electrodes for bulk electrolysis in O_2-saturated 0.05 M H_2SO_4 solution (pH 1.20). 5 min epoxy (Devcon) was used to define the geometric area of the working electrodes (~1 cm^2_{geo}). A graphite rod and a Hg/Hg_2SO_4 (saturated K_2SO_4) electrode was used as the counter electrode and the reference electrode, respectively. A two-compartment three-electrode H-cell setup

was used to avoid the oxidation of H_2O_2 product on the counter electrode. A minimal volume (3–4 mL) of electrolyte solution was used and vigorously stirred at 1200 rpm in the working electrode compartment to achieve higher H_2O_2 concentrations under facilitated mass transfer of oxygen gas. The working electrodes were operated at the constant potential of 0.5 V vs. RHE. During each run of bulk electrolysis, a small aliquot of electrolyte solution was periodically sampled from the working electrode compartment and titrated with the stock solution of $Ce(SO_4)_2$ in 0.5 M H_2SO_4 for UV-vis spectrophotometric detection of the produced H_2O_2. Detailed calculations of cumulative H_2O_2 concentration, H_2O_2 yield, Faradaic efficiency, and average catalyst leaching rate are described in the ESI†.

Electro-Fenton Degradation of Model Organic Pollutant

Electron-Fenton degradation tests were conducted in a two-compartment three-electrode H-cell (same as bulk electrolysis experiments) using Rhodamine B (RhB) (≥95%) as a model organic pollutant and *o*-$CoSe_2$/CFP (~370 $\mu g_{Co}/cm^2_{geo}$; ~1 cm^2_{geo}) as the working cathode which was operated at the constant potential of 0.5 V vs. RHE. O_2-saturated acidified 0.5 M Na_2SO_4 (pH 2.85) was used as the electrolyte solution to maintain the optimal acidic pH for the Fenton's reaction. Both RhB (20 or 40 mg/L) and Fe^{2+} (0.5 mM) were added only to the electrolyte solution in the working electrode compartment which was vigorous stirred (1200 rpm). During each electro-Fenton degradation test, a small aliquot of electrolyte solution was periodically sampled from the working electrode compartment and quantitatively diluted with the stock solution of acidified 0.5 M Na_2SO_4 (pH 2.85) for UV-vis spectrophotometric determination of the organic dye concentration.

Conflicts of interest

There are no conflicts to declare.

Acknowledgements

This research was partially supported by the National Science Foundation (NSF) Grant DMR-1508558 (H.S., D.K., and S.J.) for the materials synthesis, by the University of Wisconsin-Madison UW2020 project and the NSF Grant CHE-1955074 (H.S., R.D.R., and S.J.) for the electrochemical characterization, and by the NSF Grant CHE-120088 and CHE-1955074 (A.N.J. and J.R.S.) for the computational modelling. J.H. and B.S. thank the China Scholarship Council (CSC) for support. This research used resources of the Advanced Photon Source (APS), a U.S. Department of Energy (DOE) Office of Science User Facility operated for the DOE Office of Science by Argonne National Laboratory under Contract No. DE-AC02-06CH11357. We thank Prof. Carlo Segre and Dr. John Katsoudas for their help with the XAS measurements performed at the APS Beamline 10-BM-B. We thank Dr. Pamela Doolittle for her help with the use of ICP-MS instrument, which was acquired from Shimadzu Scientific Instruments (Columbia, MD) utilizing a grant provided as part of Shimadzu's Academic Grant Program. The authors gratefully acknowledge use of facilities and instrumentation at the UW-Madison Wisconsin Centers for Nanoscale Technology (wcnt.wisc.edu) partially supported by the NSF through the University of Wisconsin Materials Research Science and Engineering Center (DMR-1720415).

References

1. List N: Disinfectants for Use Against SARS-CoV-2. U.S. Environmental Protection Agency, https://www.epa.gov/pesticide-registration/list-n-disinfectants-use-against-sars-cov-2, (accessed April 14, 2020).
2. R. Ciriminna, L. Albanese, F. Meneguzzo and M. Pagliaro, *ChemSusChem*, 2016, **9**, 3374.
3. J. M. Campos-Martin, G. Blanco-Brieva and J. L. G. Fierro, *Angew. Chem. Int. Ed.*, 2006, **45**, 6962.
4. S. Yang, A. Verdaguer-Casadevall, L. Arnarson, L. Silvioli, V. Čolić, R. Frydendal, J. Rossmeisl, I. Chorkendorff and I. E. L. Stephens, *ACS Catal.*, 2018, **8**, 4064.
5. Y. Jiang, P. Ni, C. Chen, Y. Lu, P. Yang, B. Kong, A. Fisher and X. Wang, *Adv. Energy Mater.*, 2018, **8**, 1801909.
6. S. C. Perry, D. Pangotra, L. Vieira, L.-I. Csepei, V. Sieber, L. Wang, C. Ponce de León and F. C. Walsh, *Nat. Rev. Chem.*, 2019, **3**, 442.
7. Z. Qiang, J.-H. Chang and C.-P. Huang, *Water Res.*, 2002, **36**, 85.
8. J. K. Edwards, S. J. Freakley, R. J. Lewis, J. C. Pritchard and G. J. Hutchings, *Catal. Today*, 2015, **248**, 3.
9. S. J. Freakley, Q. He, J. H. Harrhy, L. Lu, D. A. Crole, D. J. Morgan, E. N. Ntainjua, J. K. Edwards, A. F. Carley, A. Y. Borisevich, C. J. Kiely and G. J. Hutchings, *Science*, 2016, **351**, 965.
10. S. Chu, Y. Cui and N. Liu, *Nat. Mater.*, 2017, **16**, 16.
11. Z. W. Seh, J. Kibsgaard, C. F. Dickens, I. Chorkendorff, J. K. Nørskov and T. F. Jaramillo, *Science*, 2017, **355**, eaad4998.
12. A. T. Murray, S. Voskian, M. Schreier, T. A. Hatton and Y. Surendranath, *Joule*, 2019, **3**, 2942.
13. Z. Lu, G. Chen, S. Siahrostami, Z. Chen, K. Liu, J. Xie, L. Liao, T. Wu, D. Lin, Y. Liu, T. F. Jaramillo, J. K. Nørskov and Y. Cui, *Nat. Catal.*, 2018, **1**, 156.
14. H. W. Kim, M. B. Ross, N. Kornienko, L. Zhang, J. Guo, P. Yang and B. D. McCloskey, *Nat. Catal.*, 2018, **1**, 282.
15. C. Xia, Y. Xia, P. Zhu, L. Fan and H. Wang, *Science*, 2019, **366**, 226.
16. F. Hasché, M. Oezaslan, P. Strasser and T.-P. Fellinger, *J. Energy Chem.*, 2016, **25**, 251.
17. D. Iglesias, A. Giuliani, M. Melchionna, S. Marchesan, A. Criado, L. Nasi, M. Bevilacqua, C. Tavagnacco, F. Vizza, M. Prato and P. Fornasiero, *Chem*, 2018, **4**, 106.
18. Y. Sun, I. Sinev, W. Ju, A. Bergmann, S. Dresp, S. Kühl, C. Spöri, H. Schmies, H. Wang, D. Bernsmeier, B. Paul, R. Schmack, R. Kraehnert, B. Roldan Cuenya and P. Strasser, *ACS Catal.*, 2018, **8**, 2844.
19. Y. Sun, L. Silvioli, N. R. Sahraie, W. Ju, J. Li, A. Zitolo, S. Li, A. Bagger, L. Arnarson, X. Wang, T. Moeller, D. Bernsmeier, J. Rossmeisl, F. Jaouen and P. Strasser, *J. Am. Chem. Soc.*, 2019, **141**, 12372.
20. K. Jiang, S. Back, A. J. Akey, C. Xia, Y. Hu, W. Liang, D. Schaak, E. Stavitski, J. K. Nørskov, S. Siahrostami and H. Wang, *Nat. Commun.*, 2019, **10**, 3997.

21. E. Jung, H. Shin, B.-H. Lee, V. Efremov, S. Lee, H. S. Lee, J. Kim, W. Hooch Antink, S. Park, K.-S. Lee, S.-P. Cho, J. S. Yoo, Y.-E. Sung and T. Hyeon, *Nat. Mater.*, 2020, **19**, 436.
22. J. Gao, H. b. Yang, X. Huang, S.-F. Hung, W. Cai, C. Jia, S. Miao, H. M. Chen, X. Yang, Y. Huang, T. Zhang and B. Liu, *Chem*, 2020, **6**, 658.
23. C. Tang, Y. Jiao, B. Shi, J.-N. Liu, Z. Xie, X. Chen, Q. Zhang and S. Qiao, *Angew. Chem. Int. Ed.*, **59**, 2.
24. E. Brillas, I. Sirés and M. A. Oturan, *Chem. Rev.*, 2009, **109**, 6570.
25. E. Brillas and S. Garcia-Segura, *Sep. Purif. Technol.*, 2020, **237**, 116337.
26. S. Siahrostami, A. Verdaguer-Casadevall, M. Karamad, D. Deiana, P. Malacrida, B. Wickman, M. Escudero-Escribano, E. A. Paoli, R. Frydendal, T. W. Hansen, I. Chorkendorff, I. E. L. Stephens and J. Rossmeisl, *Nat. Mater.*, 2013, **12**, 1137.
27. A. Verdaguer-Casadevall, D. Deiana, M. Karamad, S. Siahrostami, P. Malacrida, T. W. Hansen, J. Rossmeisl, I. Chorkendorff and I. E. L. Stephens, *Nano Lett.*, 2014, **14**, 1603.
28. H. Sheng, E. D. Hermes, X. Yang, D. Ying, A. N. Janes, W. Li, J. R. Schmidt and S. Jin, *ACS Catal.*, 2019, **9**, 8433.
29. D. Kong, H. Wang, Z. Lu and Y. Cui, *J. Am. Chem. Soc.*, 2014, **136**, 4897.
30. X.-L. Zhang, S.-J. Hu, Y.-R. Zheng, R. Wu, F.-Y. Gao, P.-P. Yang, Z.-Z. Niu, C. Gu, X. Yu, X.-S. Zheng, C. Ma, X. Zheng, J.-F. Zhu, M.-R. Gao and S.-H. Yu, *Nat. Commun.*, 2019, **10**, 5338.
31. M. S. Faber, R. Dziedzic, M. A. Lukowski, N. S. Kaiser, Q. Ding and S. Jin, *J. Am. Chem. Soc.*, 2014, **136**, 10053.
32. M. Cabán-Acevedo, M. L. Stone, J. R. Schmidt, J. G. Thomas, Q. Ding, H.-C. Chang, M.-L. Tsai, J.-H. He and S. Jin, *Nat. Mater.*, 2015, **14**, 1245.
33. W. Liu, E. Hu, H. Jiang, Y. Xiang, Z. Weng, M. Li, Q. Fan, X. Yu, E. I. Altman and H. Wang, *Nat. Commun.*, 2016, **7**, 10771.
34. The Materials Project, https://materialsproject.org/, (accessed April 14, 2020).
35. A. K. Singh, L. Zhou, A. Shinde, S. K. Suram, J. H. Montoya, D. Winston, J. M. Gregoire and K. A. Persson, *Chem. Mater.*, 2017, **29**, 10159.
36. W.-W. Zhao, P. Bothra, Z. Lu, Y. Li, L.-P. Mei, K. Liu, Z. Zhao, G. Chen, S. Back, S. Siahrostami, A. Kulkarni, J. K. Nørskov, M. Bajdich and Y. Cui, *ACS Appl. Energy Mater.*, 2019, **2**, 8605.
37. O. Vinogradova, D. Krishnamurthy, V. Pande and V. Viswanathan, *Langmuir*, 2018, **34**, 12259.
38. H. A. Hansen, J. Rossmeisl and J. K. Nørskov, *Phys. Chem. Chem. Phys.*, 2008, **10**, 3722.
39. J. K. Nørskov, J. Rossmeisl, A. Logadottir, L. Lindqvist, J. R. Kitchin, T. Bligaard and H. Jónsson, *J. Phys. Chem. B*, 2004, **108**, 17886.
40. V. Viswanathan, H. A. Hansen, J. Rossmeisl and J. K. Nørskov, *J. Phys. Chem. Lett.*, 2012, **3**, 2948.
41. A. Kulkarni, S. Siahrostami, A. Patel and J. K. Nørskov, *Chem. Rev.*, 2018, **118**, 2302.
42. D. C. Ford, A. U. Nilekar, Y. Xu and M. Mavrikakis, *Surf. Sci.*, 2010, **604**, 1565.
43. P. Chen, K. Xu, S. Tao, T. Zhou, Y. Tong, H. Ding, L. Zhang, W. Chu, C. Wu and Y. Xie, *Adv. Mater.*, 2016, **28**, 7527.
44. M. M. Butala, V. V. T. Doan-Nguyen, A. J. Lehner, C. Göbel, M. A. Lumley, S. Arnon, K. M. Wiaderek, O. J. Borkiewicz, K. W. Chapman, P. J. Chupas, M. Balasubramanian and R. Seshadri, *J. Phys. Chem. C*, 2018, **122**.
45. Y. Zhu, H.-C. Chen, C.-S. Hsu, T.-S. Lin, C.-J. Chang, S.-C. Chang, L.-D. Tsai and H. M. Chen, *ACS Energy Lett.*, 2019, **4**.
46. E. Pizzutilo, O. Kasian, C. H. Choi, S. Cherevko, G. J. Hutchings, K. J. J. Mayrhofer and S. J. Freakley, *Chem. Phys. Lett.*, 2017, **683**, 436.
47. C. H. Choi, M. Kim, H. C. Kwon, S. J. Cho, S. Yun, H.-T. Kim, K. J. J. Mayrhofer, H. Kim and M. Choi, *Nat. Commun.*, 2016, **7**, 10922.
48. S. Yang, J. Kim, Y. J. Tak, A. Soon and H. Lee, *Angew. Chem. Int. Ed.*, 2016, **55**, 2058.
49. R. Shen, W. Chen, Q. Peng, S. Lu, L. Zheng, X. Cao, Y. Wang, W. Zhu, J. Zhang, Z. Zhuang, C. Chen, D. Wang and Y. Li, *Chem*, 2019, **5**, 2099.
50. J. Zhang, K. Sasaki, E. Sutter and R. R. Adzic, *Science*, 2007, **315**, 220.
51. J. Kibsgaard, Y. Gorlin, Z. Chen and T. F. Jaramillo, *J. Am. Chem. Soc.*, 2012, **134**, 7758.
52. E. Brillas, J. C. Calpe and J. Casado, *Water Res.*, 2000, **34**, 2253.
53. E. Brillas, E. Mur, R. Sauleda, L. Sànchez, J. Peral, X. Domènech and J. Casado, *Appl. Catal. B*, 1998, **16**, 31.
54. M. A. Oturan, J. Peiroten, P. Chartrin and A. J. Acher, *Environ. Sci. Technol.*, 2000, **34**, 3474.
55. S. Yuan, Y. Fan, Y. Zhang, M. Tong and P. Liao, *Environ. Sci. Technol.*, 2011, **45**, 8514.
56. G. Kresse and J. Hafner, *Phys. Rev. B*, 1993, **47**, 558.
57. G. Kresse and J. Hafner, *Phys. Rev. B*, 1994, **49**, 14251.
58. G. Kresse and J. Furthmüller, *Comput. Mater. Sci.*, 1996, **6**, 15.
59. G. Kresse and J. Furthmüller, *Phys. Rev. B*, 1996, **54**, 11169.
60. S. R. Bahn and K. W. Jacobsen, *Comput. Sci. Eng.*, 2002, **4**, 56.
61. P. E. Blöchl, *Phys. Rev. B*, 1994, **50**, 17953.
62. G. Kresse and D. Joubert, *Phys. Rev. B*, 1999, **59**, 1758.
63. J. P. Perdew, K. Burke and M. Ernzerhof, *Phys. Rev. Lett.*, 1996, **77**, 3865.
64. J. P. Perdew, K. Burke and M. Ernzerhof, *Phys. Rev. Lett.*, 1997, **78**, 1396.
65. S. Grimme, J. Antony, S. Ehrlich and H. Krieg, *J. Chem. Phys.*, 2010, **132**, 154104.
66. V. I. Anisimov, J. Zaanen and O. K. Andersen, *Phys. Rev. B*, 1991, **44**, 943.
67. X. Wu, S. Han, D. He, C. Yu, C. Lei, W. Liu, G. Zheng, X. Zhang and L. Lei, *ACS Sustain. Chem. Eng.*, 2018, **6**, 8672.
68. K. Mathew, R. Sundararaman, K. Letchworth-Weaver, T. A. Arias and R. G. Hennig, *J. Chem. Phys.*, 2014, **140**, 084106.
69. K. Mathew, R. G. Hennig and J. Bértoli, 2019, DOI: 10.5281/zenodo.2555053.
70. H. J. Monkhorst and J. D. Pack, *Phys. Rev. B*, 1976, **13**, 5188.
71. A. B. Alchagirov, J. P. Perdew, J. C. Boettger, R. C. Albers and C. Fiolhais, *Phys. Rev. B*, 2001, **63**, 224115.
72. G. Henkelman, B. P. Uberuaga and H. Jónsson, *J. Chem. Phys.*, 2000, **113**, 9901.
73. G. Henkelman, G. Jóhannesson and H. Jónsson, in *Theoretical Methods in Condensed Phase Chemistry*, ed. S. D. Schwartz, Kluwer Academic Publishers, 2002, vol. 5, ch. 10, pp. 269-302.
74. G. Henkelman and H. Jónsson, *J. Chem. Phys.*, 1999, **111**, 7010.

75. A. Heyden, A. T. Bell and F. J. Keil, *J. Chem. Phys.*, 2005, **123**, 224101.
76. J. Kästner and P. Sherwood, *J. Chem. Phys.*, 2008, **128**, 014106.
77. NIST Chemistry WebBook, https://webbook.nist.gov/cgi/cbook.cgi?ID=C7722841&Mask=10#Solubility, (accessed April 14, 2020).
78. B. Ravel and M. Newville, *J. Synchrotron Radiat.*, 2005, **12**, 537.